Radial integration boundary element method for two-dimensional non-homogeneous convection-diffusion-reaction problems with variable source term

Salam Adel AL-Bayati[a], Luiz C. Wrobel[b,*]

[a] *College of Engineering, Design and Physical Sciences, Brunel University London, Uxbridge, UB8 3PH, UK*
[b] *Institute of Materials and Manufacturing, Brunel University London, Uxbridge, UB8 3PH, UK*

Abstract

This paper describes a new formulation of the radial integration boundary element method (RIBEM) for two-dimensional non-homogeneous convection-diffusion-reaction problems with variable source terms. The radial integration method (RIM) is implemented to transform the resulting domain integral into equivalent boundary integrals, and thus a boundary-only integral equation formulation can be achieved. The fundamental solution of the steady-state convection-diffusion-reaction equation with constant coefficients is employed. The integral representation formula for the convection-diffusion-reaction problem with source term is obtained from Green's second identity. Numerical applications are included for five different cases, for which analytical solutions are available, to establish the validity of the proposed approach and to demonstrate convergence and efficiency of the proposed technique. Results obtained show that the RIBEM produced an excellent agreement with the analytical solutions and the results do not present oscillations or damping of the wave front, as may appear in other numerical techniques.

Keywords: Convection-diffusion-reaction problem; Radial integration method; Boundary element method; Source term; Domain integral

1. Introduction

A simple and robust transformation technique, called the radial integration method (RIM), was developed by Gao [1] which not only can transform any complicated domain integral to the boundary without using particular solutions, but can also remove various singularities appearing in the domain integrals [2, 3].

Based on the RIM, the RIBEM was developed and applied to handle a wide range of engineering and mathematical problems including non-homogeneous steady-state and transient heat conduction problems, acoustics problems, diffusion problems, elastoplasticity and other mechanical problems [1, 4, 5, 6, 7, 8, 9].

Yang and Gao [10] proposed a new boundary element technique to handle transient heat conduction problems, for which the RIM is implemented to transfer the domain integral associated with the time derivative of temperatures, and the radial integral is evaluated numerically. The RIM can be applied to

*Corresponding author,
Email addresses: Salam.AL-Bayati@brunel.ac.uk (Salam Adel AL-Bayati), Luiz.Wrobel@brunel.ac.uk (Luiz C. Wrobel)

the combination of power series expansion operated on the parameter plane of intrinsic coordinates [11] or for the projection plane of global coordinates [12, 13], for which it can evaluate different types of singular boundary integrals numerically [14].

Recently, Feng [15] proposed a new type of single integral equation technique to solve transient heat conduction problems in multi-media with variable thermal properties. The same author has also derived an interface integral equation method to solve general multi-media mechanical problems by considering the discontinuity of the stress-strain constitutive relationship during the transformation from elastic to plastic regions [16]. Feng also proposed a new BEM formulation without initial stresses for solving two and three-dimensional elastoplastic problems [17].

Yang *et al*. [18, 19] successfully derived a series of analytical expressions for evaluating radial integrals, which are utilised in the RIM for converting the domain integrals into equivalent boundary integrals. By using these analytical expressions, the computation time spent in the numerical calculation of radial integrals can be considerably reduced. This technique has been implemented to handle non-homogeneous heat conduction, non-homogeneous elasticity and thermoelasticity problems. However, in the derivation of the analytical radial integral expressions, some special circumstances may appear which will influence the accuracy of the results [14].

The RIBEM was successfully derived and implemented for the free vibration analysis of anisotropic plates [20], and to thermoelasticity, elastic inclusion problems, creep damage mechanics problems, transient heat conduction problems, and viscous flow problems [9, 21, 22, 23, 24]. Owing to the advantages of the RIM, mainly that particular solutions are not required and various domain integrals appearing in the same integral equation can be dealt with simultaneously, RIM-based BEMs have gained considerable attention from many BEM researchers [25, 26, 27].

The radial integral in the RIBEM formulation is usually calculated by utilising Gaussian quadrature, which requires it to be computed at each Gaussian point of the boundary element under consideration. Evaluating the radial integrals numerically, especially for a three-dimensional non-linear and large-scale non-homogeneous problem, is highly time-consuming and this will lead to a reduction of the performance and the efficiency of this numerical method [17, 24].

A brief outline of this paper is as follows: Section 2 shows the representation of the non-homogeneous convection-diffusion-reaction equation with source term. Section 3 derives the boundary element formulation of the governing equation using the fundamental solution of the corresponding equation without a source. In section 4, the RIM formulation is developed for the 2D non-homogeneous convection-diffusion-reaction problem with source term, followed in section 5 by domain integrals with weakly-singular integrand for this model. Space discretisation of the RIBEM formulation for the corresponding problem is discussed in section 6, while section 7 gives a description of the assembly of the RIBEM system. Section 8 compares and discusses the solution profiles for the present numerical experiments with the analytical solution of the tested cases. Some error indicators were used to represent the convergence rate and the solution behaviour.

Computational aspects are included to demonstrate the performance of this approach in section 9. Finally, some conclusions and remarks are provided in the last section.

2. Non-homogeneous convection-diffusion-reaction problem with source term

The solution of convection-diffusion-reaction problems is a difficult task for all numerical methods because of the nature of the governing equation, which includes first-order and second-order partial derivatives in space [28, 29, 30, 31, 32]. The convection-diffusion-reaction equation with source term is the basis of many physical and chemical phenomena, and its use has also spread into economics, financial forecasting and other fields [33].

Our mathematical model, i.e. non-homogeneous two-dimensional convection-diffusion-reaction problem with source term over a domain Ω in R^2 limited by a boundary Γ, for isotropic materials, is governed by the following partial differential equation:

$$D\nabla^2\phi\left(x,y\right) - v_x\frac{\partial\phi\left(x,y\right)}{\partial x} - v_y\frac{\partial\phi\left(x,y\right)}{\partial y} - k\,\phi\left(x,y\right) = S\left(x,y\right) \tag{1}$$

$$x, y \in \Omega \subset R^d$$

In Eq.(1), ϕ represents the concentration of a substance, treated as a function of space, Γ is a bounded domain in R^d, d is the dimension of the problem. The velocity components v_x and v_y along the x and y directions are assumed to be constant in space. Besides, D is the diffusivity coefficient, k represents the first-order reaction constant or adsorption coefficient and $S\left(x,y\right)$ represents the source term. The boundary conditions are

$$\phi = \bar{\phi} \quad \text{over} \quad \Gamma_D \tag{2}$$

$$q = \frac{\partial\phi}{\partial n} = \bar{q} \quad \text{over} \quad \Gamma_N \tag{3}$$

where Γ_D and Γ_N are the Dirichlet (essential) and Neumann (natural) parts of the boundary with $\Gamma = \Gamma_D \cup \Gamma_N$, and $\Gamma_D \cap \Gamma_N = \emptyset$ (see Fig. 1). The parameter that describes the relative influence of the convective and diffusive components is called Péclet number, Pé $= |v|\,L/D$, where $v = \left(v_x^2 + v_y^2\right)^{1/2}$ is the velocity and L is a characteristic length of the domain. For small values of Pé, Eq.(1) behaves as a parabolic differential equation, while for large values the equation becomes more like hyperbolic. These changes in the structure of the differential equation according to the value of the Péclet number have significant effects on its numerical solution.

3. Boundary element formulation of non-homogeneous convection-diffusion-reaction problems with source term

Let us consider a region $\Omega \subset R^2$ bounded by a piecewise smooth boundary Γ. The transport of ϕ in the presence of a reaction term is governed by the two-dimensional convection-diffusion-reaction Eq.(1).

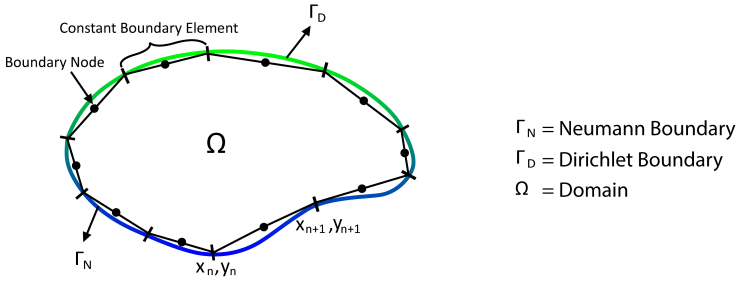

Figure 1: Definition of domain, boundary, and constant boundary elements

The variable ϕ can be interpreted as temperature for heat transfer problems, concentration for dispersion problems, etc, and will be herein referred to as a concentration. For the sake of obtaining an integral equation equivalent to the partial differential equation (1), a fundamental solution of Eq.(1) is necessary. Equation (1) can be transformed into an equivalent integral equation by applying a weighted residual technique. Starting with the weighted residual statement:

$$\int_{\Omega} \left(D\nabla^2 \phi\left(x,y\right) - v_x \frac{\partial \phi\left(x,y\right)}{\partial x} - v_y \frac{\partial \phi\left(x,y\right)}{\partial y} - k\,\phi\left(x,y\right) \right) \phi^* d\Omega = \int_{\Omega} S\left(x,y\right) \phi^* d\Omega \tag{4}$$

and integrating by parts twice the Laplacian and once the first-order derivatives, the following equation is obtained:

$$\phi\left(\xi\right) = D \int_{\Gamma} \phi^* \frac{\partial \phi}{\partial n}\, d\Gamma - D \int_{\Gamma} \phi\, \frac{\partial \phi^*}{\partial n}\, d\Gamma - \int_{\Gamma} \phi\, \phi^*\, \bar{v}_n\, d\Gamma - \int_{\Omega} S\left(x,y\right) \phi^*\, d\Omega \tag{5}$$

where $\bar{v}_n = \mathbf{v}.\mathbf{n}$, $\mathbf{n}$ is the unit outward normal vector and the dot stands for scalar product. In the above equation, ϕ^* is the fundamental solution of the convection-diffusion-reaction equation without source term. For two-dimensional problems, ϕ^* is of the form

$$\phi^*\left(\xi,\chi\right) = \frac{1}{2\pi D} \exp^{-\left(\frac{v.r}{2D}\right)} K_0\left(\mu r\right) \tag{6}$$

where

$$\mu = \left[\left(\frac{\bar{v}}{2D} \right)^2 + \frac{k}{D} \right]^{\frac{1}{2}} \tag{7}$$

in which ξ and χ are the source and field points, respectively, and r is the modulus of $\mathbf{r}$, the distance vector between the source and field points. The derivative of the fundamental solution with respect to the outward normal direction is given by

$$\frac{\partial \phi^*}{\partial n} = \frac{1}{2\pi D} \exp^{-\left(\frac{\bar{v}.r}{2D}\right)} \left[-\mu\, K_1\left(\mu r\right) \frac{\partial r}{\partial n} - \frac{\bar{v}_n}{2D} K_0\left(\mu r\right) \right] \tag{8}$$

In the above, K_0 and K_1 are Bessel functions of second kind, of orders zero and one, respectively. The exponential term is responsible for the inclusion of the correct amount of 'upwind' into the formulation [34]. Expression (5) is valid for source points ξ inside the domain Ω. A similar expression can be obtained, by a

limit analysis, for source points ξ on the boundary Γ, in the form

$$c\left(\xi\right)\phi\left(\xi\right) = D\int_{\Gamma}\phi^{*}\frac{\partial\phi}{\partial n}\,d\Gamma \;-\; D\int_{\Gamma}\phi\;\frac{\partial\phi^{*}}{\partial n}\,d\Gamma - \int_{\Gamma}\phi\,\phi^{*}\,\bar{v}_{n}\;d\Gamma \;-\; \int_{\Omega}S\left(x,y\right)\phi^{*}\,d\Omega \tag{9}$$

in which $c\left(\xi\right)$ is a function of the internal angle the boundary Γ makes at point ξ [32].

4. The radial integration method for transforming general domain integrals to the boundary

Given a two-dimensional domain Ω bounded by a boundary Γ, define a Cartesian coordinate system (χ_1, χ_2) and a polar coordinate system (r, θ) with origin at the source point $\xi = (\xi_1, \xi_2)$. The relationships between the Cartesian and polar coordinate systems are:

$$\begin{aligned} r_1 &= \chi_1 - \xi_1 = r\cos\left(\theta\right) \\ r_2 &= \chi_2 - \xi_2 = r\sin\left(\theta\right) \end{aligned} \tag{10}$$

where $0 \leq \theta \leq 2\pi$ and r is the distance between the source point ξ and a field point χ. The relationship between a differential domain in the Cartesian system and the polar system is given by

$$d\Omega = d\chi_1\, d\chi_2 = J\, dr\, d\theta = r\, dr\, d\theta \tag{11}$$

where $J = \left|\partial\left(\chi_1, \chi_2\right)/\partial\left(r, \theta\right)\right| = r$ is the Jacobian. We can notice from Fig. 2 that when the field point is located on the boundary, we can obtain the following relation [35]

$$r d\theta = d\Gamma\, cos\varphi = d\Gamma\,\frac{r_i n_i}{r} \tag{12}$$

where φ is the angle between the normal of the differential arc $r d\theta$ with radius r with the differential boundary Γ with outward normal n_i, with the summation subscript i taking the values 1 to 2. Substituting Eq.(12) in (11) and re-arranging, we obtain

$$d\Omega = r\, dr\, ds \tag{13}$$

where

$$ds = \frac{1}{r}\frac{\partial r}{\partial n}d\Gamma \tag{14}$$

for which the following expressions are employed

$$\frac{\partial r}{\partial n} = r_{,i}n_i \tag{15}$$

$$r_{,i} = \frac{\partial r}{\partial \chi_i} = \frac{r_i}{r} = \frac{\left(\chi_i - \xi_i\right)}{r} \tag{16}$$

$$r_{,i}r_{,i} = 1 \tag{17}$$

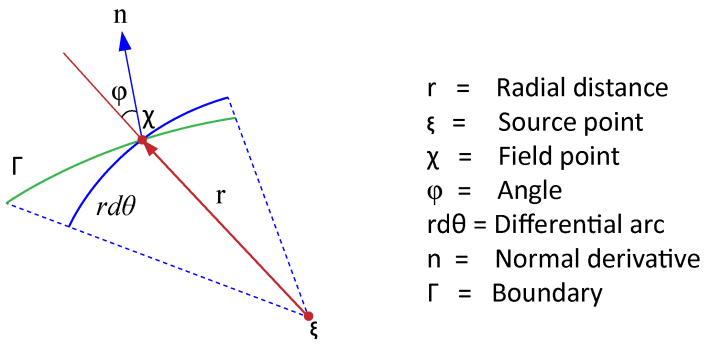

Figure 2: Relationship between differential elements $rd\theta$ and $d\Gamma$

Now, a function in Cartesian coordinates can be written in polar coordinates and integrated as follows:

$$\int_{\Omega} f(\chi)\, d\Omega = \int_{s} \left\{ \int_{0}^{r(\chi)} f(\chi)\, r^{\alpha} dr \right\} ds(\chi) = \int_{s} F(\chi)\, ds(\chi) \tag{18}$$

where

$$F(\chi) = \int_{0}^{r(\chi)} f(\chi)\, r^{\alpha} dr \tag{19}$$

In Eqs.(18) and (19), $\alpha = 1$ for the two-dimensional case and $\alpha = 2$ for the three-dimensional case. The symbol $f(\chi)$ means the variable f takes values on the boundary Γ (see Fig. 2). Substituting expression (14) into (18), we obtain

$$\int_{\Omega} f(\chi)\, d\Omega = \int_{\Gamma} \frac{1}{r^{\alpha}} \frac{\partial r}{\partial n} F(\chi)\, d\Gamma(\chi) \tag{20}$$

The following notes are crucial for the RIM, especially for Eqs.(19) and (20):

- Although the derivation is in a polar coordinate system, the variables are now operated in the Cartesian coordinate system.
- The equations are valid for a source point ξ located at both internal and boundary nodes.
- The most attractive feature of the RIM is that the transformation (20) is very simple and has similar forms for both 2D and 3D. It can remove various singularities appearing in domain integrals since r^{α} is included in the radial integral in expression (19).

  In order to transform a domain integral to a boundary one, the main task is to calculate the radial integral in Eq.(20), which can be done analytically for simple kernels. We have written a simple Matlab code for analytical integration of Eq.(20) which can integrate many given functions $f(\chi)$, however, for complicated functions, numerical integration techniques are required [2, 3].
- In order to evaluate the RIM in Eq.(19), the coordinates χ_1, χ_2 in $f(\chi)$ need to be expressed in terms of the distance r using:

$$\chi_i = \xi_i + r_{,i}\, r; \quad i = 1, 2. \tag{21}$$

where the quantities ξ_i and $r_{,i}$ are constants for the radial integral in Eq.(19).

- Weak singularities involved in the integrand $f(\chi)$ have been transformed to the boundary. Consequently, no singularities exist at internal nodes for such integrands.

- Expression (20) can be computed using constant, linear and higher-order boundary elements in the same way as in the standard BEM.

5. RIM formulation for domain integrals with weakly-singular integrand

It is known that, in a domain integral, if the integrand includes the term $1/r^{\alpha}$, then when $n \leq \alpha$ ($\alpha = 1$) in 2D and ($\alpha = 2$) in 3D, this integrand is weakly singular as the source point approaches the field point. For such an integrand, Eq.(19) shows that the singularity is explicitly eliminated after multiplying by the term r^{α}. After integrating Eq.(19), $F(\chi)$ will include a term r^m where m is equal to or greater than 1. This makes the transformed boundary integral (20) weakly singular when the source point approaches the boundary. For strongly singular integrands $f(\chi)$, which includes $1/r^n$ with $n > 1$, Eq.(19) cannot omit the singularity completely. However, for some special functions, for example the strain kernels in elastoplastic integral equations, the idea of differentiating Eqs.(20) and (19) can be utilised to remove the strong singularities [35].

From Eqs.(19) and (20), we can see that the key task for the transformation of domain to boundary integrals is the evaluation of the radial integral (19). For most kernel functions involved in domain integrals in BEM for mechanical and potential problems, Eq.(19) can be analytically integrated. For some very complicated functions, it may be difficult to do this. In that case, numerical integration techniques, such as Gaussian quadrature, may be used to compute the radial integral for every field point χ. To use Gaussian quadrature, the following variable transformation is required:

$$r = \frac{r(\chi)}{2}\eta + \frac{r(\chi)}{2}, \ (-1 \leq \eta \leq 1) \tag{22}$$

When the source term $S(x, y)$ is variable, then the RIM can be implemented to transform the domain integral appearing in Eq.(5). The radial integral can be evaluated by direct implementation (analytically) as described in section 4 when the source term is constant whilst for variable source terms, numerical integration will be implemented. Using Eqs.(21) and (22), the radial integral (19) can be expressed as:

$$\begin{aligned} F(\chi) &= \int_{-1}^{+1} f(\chi(\eta)) \left(\frac{r(\chi)}{2}\eta + \frac{r(\chi)}{2}\right)^{\alpha} \frac{r(\chi)}{2} d\eta \\ &= \left(\frac{r(\chi)}{2}\right)^{\alpha+1} \sum_{n=1}^{N_g} (1+\eta_n)^{\alpha} f(\chi(\eta_n)) w_n \end{aligned} \tag{23}$$

where N_g is the number of Gaussian points, η_n are the Gaussian point coordinates and w_n is the associated weight. In this work, 60 Gauss points are used for increased accuracy.

6. Space discretisation of the RIBEM formulation for 2D convection-diffusion-reaction model with source term

For numerical solution of the problem, Eq.(9) can be written in discretised form in which the integrals over the boundary are approximated by a summation of integrals over individual boundary elements, i.e.

$$c_i\,\phi_i = D\sum_{j=1}^{N}\int_{\Gamma_j}\phi^*\,\frac{\partial\phi}{\partial n}\,d\Gamma\;-D\sum_{j=1}^{N}\int_{\Gamma_j}\left(\frac{\partial\phi^*}{\partial n}+\frac{v_n}{D}\,\phi^*\right)\phi\,d\Gamma$$

$$-\sum_{j=1}^{N}\int_{\Gamma_j}\left[\frac{1}{r}\,\frac{\partial r}{\partial n}\,\left(\frac{r}{2}\right)^2\sum_{n=1}^{N_g}\left(1+\xi_n\right)f\left(\chi\left(\xi_n\right)\right)w_n\right]\phi^*d\Gamma \tag{24}$$

where the index i stands for values at the source point ξ_i, N_g is the number of integration points and N the number of boundary elements. In the above expression, it can be noticed that:

$$\frac{\partial\phi^*}{\partial n}+\frac{v_n}{D}\,\phi^*=\frac{1}{2\pi D}\exp^{\left(\frac{-v.r}{2D}\right)}\left[-\mu K_1\left(\mu r\right)\frac{\partial r}{\partial n}+\frac{v_n}{2D}K_0\left(\mu r\right)\right] \tag{25}$$

Next, the constant functions ϕ and $\frac{\partial\phi}{\partial n}$ within each element are approximated by their nodal values. Therefore, the following expression is obtained

$$c_i\phi_i=\sum_{j=1}^{N}\left(G_{ij}\,q_j-H_{ij}\,\phi_j\right)+B_i \tag{26}$$

Note that the two influence matrices can be represented as:

$$G_{ij}=D\int_{\Gamma_j}\phi^*d\Gamma \tag{27}$$

and

$$H_{ij}=D\int_{\Gamma_j}\left(\frac{\partial\phi^*}{\partial n}+\frac{v_n}{D}\phi^*\right)d\Gamma \tag{28}$$

with

$$B_i=\int_{\Gamma_j}\left(\frac{1}{r}\,\frac{\partial r}{\partial n}\,\left(\frac{r}{2}\right)^2\sum_{n=1}^{N_g}\left(1+\xi_n\right)f\left(\chi\left(\xi_n\right)\right)w_n\right)\phi^*\,d\Gamma \tag{29}$$

The above expression (26) involves N values of ϕ and $q=\frac{\partial\phi}{\partial n}$, half of which are prescribed as boundary conditions. In order to calculate the remaining unknowns, it is necessary to generate N equations. This can be done by using a simple collocation technique, i.e. by making the equation be satisfied at the N nodal points. The c_i values have been incorporated into the diagonal coefficients of matrix H. After introducing the boundary conditions, the system is reordered and solved by a direct method, for instance, Gauss elimination or LU decomposition.

The result is a system of equations of the form:

$$H\phi=Gq+B \tag{30}$$

where B is the term representing the radial integral for the source term as in Eq.(5). Evaluation of the coefficients of matrices H, G and vector B is carried out numerically. It should be noted that the diagonal coefficients of matrix G have a weak singularity of the logarithmic type, and are calculated using the self-adaptive scheme of Telles [36]. The coefficients H_{ii} can be calculated, in the absence of the reaction term, by noting that a consistent solution for a prescribed uniform concentration along the boundary can be obtained if matrix H is singular, i.e.

$$H_{ii} = -\sum_{j=1}^{N} H_{ij} \ (i \neq j) \tag{31}$$

However, when $k \neq 0$, there is a flux when a uniform concentration is applied (or, in other words, the zero flux state cannot be achieved for a uniform concentration distribution). In this case, the coefficients H_{ii} have to be evaluated explicitly [37]. These terms are composed of two parts, one being a sum of integrals of the form H_{ij} and the other the free term c_i. The former also possesses a logarithmic singularity, and is calculated using Telles' scheme [36]. The free terms c_i depend only on geometry, and have the same values as for Laplace's equation [38].

7. Error norms indicators

To measure the quality of the approximation solutions, we need to utilise some appropriate error norms. In this work, we use boundary L^∞ and RMS error norms, which can be equally evaluated from the boundary solution alone in contrast to the energy norm which requires solutions to be known at internal nodes as well [39]. In what follows, all the error norms are based on the analytical solutions. In our context, there are two ways to present the solution convergence and accuracy, either by the root mean square error or by using an average relative error. Our goal here is to study the convergence rates to show accuracy and convergence of the proposed method.

To check the convergence of the proposed method, the root-mean-square (RMS) error is introduced:

$$\text{RMS} = \sqrt{\frac{1}{N}\sum_{i=1}^{N} \left|\phi_{i,numer} - \phi_{i,exact}\right|^2} \tag{32}$$

The root mean square norm is based on the difference between the simulation results ϕ_{numer} and the analytical solution ϕ_{exact}.

Finally, we can define the L^∞ error norm by:

$$L^\infty = \left\|e_\phi\right\|_\infty = \text{Max}\left|\phi_{exact} - \phi_{numer}\right| \tag{33}$$

Here, ϕ_{numer}, ϕ_{exact}, $\phi_{numer,max}$ and $\phi_{numer,min}$ represent the calculated solution value, the analytical solution value and the maximum and minimum analytical solution values in the domain, respectively. N is the total number of elements.

8. Numerical experiments and results

The present section is concerned with numerical tests of the RIBEM for the solution of two-dimensional non-homogeneous convection-diffusion-reaction problems with constant and variable source terms. We shall examine five case studies with known analytical solutions to quantitatively and qualitatively assess the convergence, accuracy and robustness of the proposed formulation. All numerical computations were coded using Matlab 2016a Version 9.

8.1. Experiment 1: Two-dimensional non-homogeneous convection-diffusion-reaction problem over a square-shaped region with constant source term

In this test, a two-dimensional transport problem with constant source term has been examined to analyse the validity of the present formulation. This problems deals with a square cross-section with unit dimensions. We assume the diffusivity $D = 1$, the reaction value $k = 0$, and velocity component $v_y = 0$. We shall consider the cases where $S = 5$, 10, 50, 100 and 500.

The mixed boundary conditions are as follows: For vertical faces, i.e. $x = 0$ and $x = 1$, Dirichlet boundary conditions are imposed:

$$\phi = 0;\ x = 0,\ 0 \leq y \leq 1$$

$$\phi = 1;\ x = 1,\ 0 \leq y \leq 1$$

and zero fluxes (Neumann boundary conditions) for the horizontal faces, i.e. $y = 0$ and $y = 1$:

$$q = \frac{\partial \phi}{\partial n} = 0;\ y = 0,\ 0 \leq x \leq 1$$

$$q = \frac{\partial \phi}{\partial n} = 0;\ y = 1,\ 0 \leq x \leq 1$$

The analytical solution of the problem is given by

$$\phi\left(x, y\right) = \phi_0 + \frac{S}{v_x} x + \frac{\phi_L - \phi_0 - \left(SL/v_x\right)}{\exp\left(\frac{v_x L}{D}\right) - 1} \left[\exp\left(\frac{v_x L\, x}{D}\right) - 1\right] \tag{34}$$

The geometry is discretised into 120 equally-spaced constant elements, 30 on each side as shown in Fig.3.

8.1.1. Positive velocity

The concentration ϕ at boundary nodes along the faces $y = 0$ and $y = 1$ is investigated. Figure 4 displays the numerical and analytical solutions along the bottom and the top sides of the channel for $S = 5$ and $v_x = 10$. Next, Fig. 5 presents RIBEM and analytical solutions for $S = 10$ and $v_x = 30$. Figure 6 presents the numerical and analytical solutions for $S = 50$ and $v_x = 15$. Figure 7 shows the numerical and exact solutions for $S = 500$ and $v_x = 20$. Figure 8 presents the solution for $S = 100$ and $v_x = 500$. Figure 9 shows the variation of the concentration profile along the horizontal faces for a high value of the source term $S = 500$ and velocity $v_x = 500$, compared to the analytical solution, in which case the Péclet number

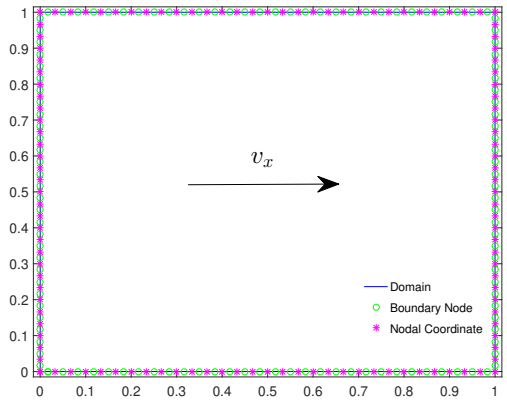

Figure 3: Geometry and model discretisation with unit side length

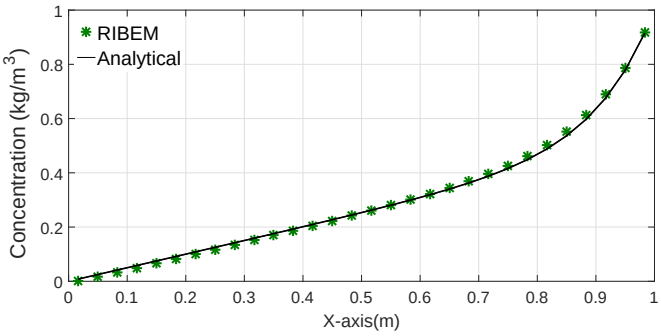

Figure 4: Variation of concentration profile ϕ along faces $y = 0$ and $y = 1$ for $S = 5$, $v_x = 10$: comparison between the analytical (solid line) and numerical (star points) solutions

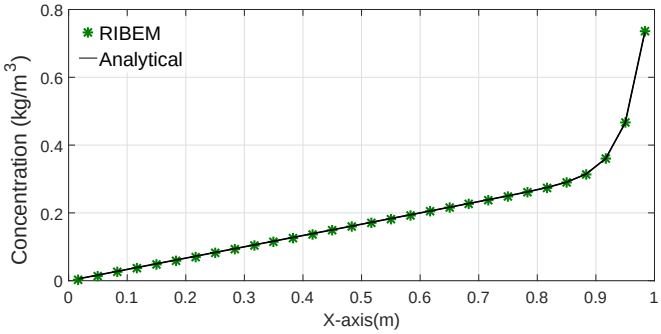

Figure 5: Variation of concentration profile ϕ along faces $y = 0$ and $y = 1$ for $S = 10$, $v_x = 30$: comparison between the analytical (solid line) and numerical (star points) solutions

is Pé = 500. All figures display the expected behaviour for the concentration profiles at different Péclet numbers and with various source term values, showing an excellent agreement with the analytical results.

To examine the variation of the concentration profiles at different positions at the bottom face, Table 1 shows the numerical and analytical solutions for $S = 50$ and $v_x = 50$.

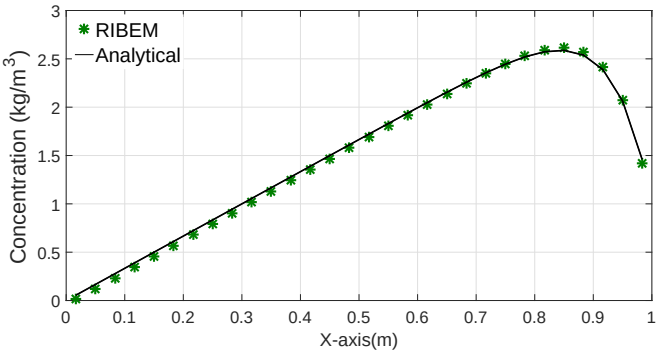

Figure 6: Variation of concentration profile ϕ along faces $y = 0$ and $y = 1$ for $S = 50$, $v_x = 15$: comparison between the analytical (solid line) and numerical (star points) solutions

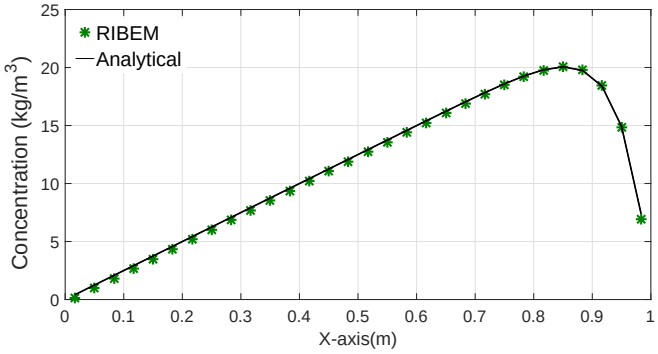

Figure 7: Variation of concentration profile ϕ along faces $y = 0$ and $y = 1$ for $S = 500$, $v_x = 20$: comparison between the analytical (solid line) and numerical (star points) solutions

Table 1: Results of RIBEM for convection-diffusion-reaction problem at Pé = 50

x	RIBEM	Analytical
0.1	0.1124	0.1167
0.2	0.2131	0.2167
0.3	0.3136	0.3167
0.4	0.4139	0.4167
0.5	0.5141	0.5167
0.6	0.6143	0.6167
0.7	0.7144	0.7167
0.8	0.8146	0.8167
0.9	0.9151	0.9167

To assess the convergence of the boundary concentrations with mesh refinement, Table 2 presents the global errors for L^∞ and RMS. The accuracy of the results for the RIBEM is very good as both the RMS

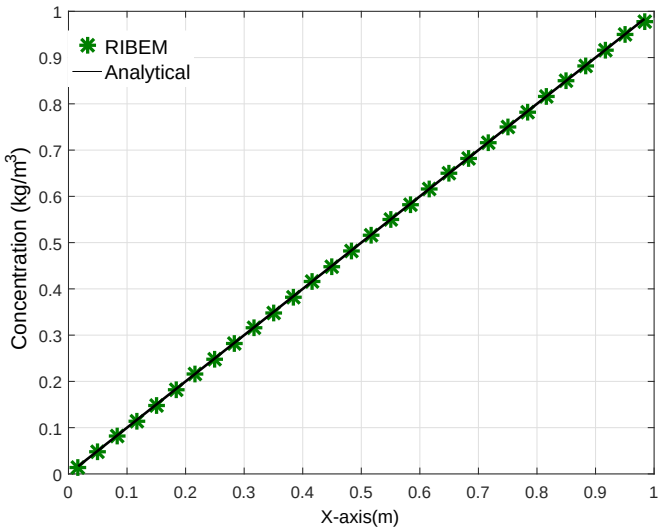

Figure 8: Variation of concentration profile ϕ along faces $y = 0$ and $y = 1$ for $S = 100$, $v_x = 500$: comparison between the analytical (solid line) and numerical (star points) solutions

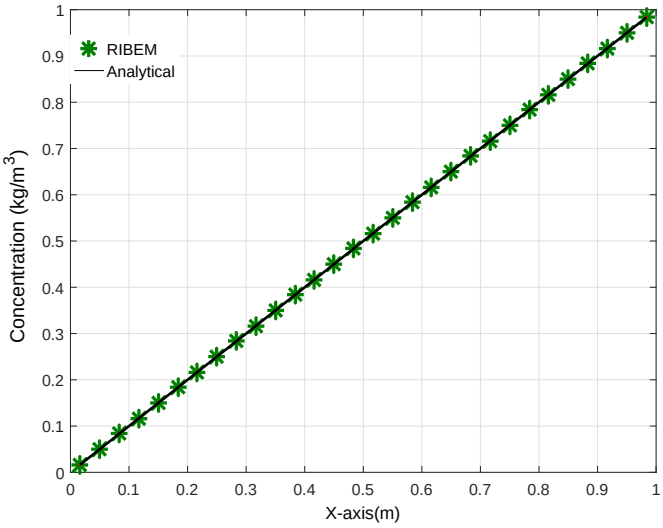

Figure 9: Variation of concentration profile ϕ along faces $y = 0$ and $y = 1$ for $S = 500$, $v_x = 500$: comparison between the analytical (solid line) and numerical (star points) solutions

error norm and the relative error in L^∞ norm are of the order 10^{-3}. The simulation and the analytical solutions on two-dimensional refined meshes are computed with good agreement. The calculated errors are cast in the RMS error norm and are plotted in Fig. 10. This comparison represents the different global error solutions for this case study.

Table 2: L^∞ and RMS norms of RIBEM for convection-diffusion-reaction problem with different values of Péclet number.

Péclet number, L^∞ and RMS error norms in ϕ, Experiment 1								
Mesh size	Pé = 15		Pé = 20		Pé = 25		Pé = 30	
	$\|e_\phi\|_\infty$	$\|e_\phi\|_{RMS}$	$\|e_\phi\|_\infty$	$\|e_\phi\|_{RMS}$	$\|e_\phi\|_\infty$	$\|e_\phi\|_{RMS}$	$\|e_\phi\|_\infty$	$\|e_\phi\|_{RMS}$
20	1.3×10^{-2}	6.4×10^{-3}	7.3×10^{-3}	3.6×10^{-3}	4.2×10^{-3}	2.2×10^{-3}	2.6×10^{-3}	1.4×10^{-3}
40	1.2×10^{-2}	5.5×10^{-3}	7.3×10^{-3}	3.3×10^{-3}	4.8×10^{-3}	2.2×10^{-3}	3.4×10^{-3}	1.6×10^{-3}
80	9.8×10^{-3}	4.8×10^{-3}	6.0×10^{-3}	2.9×10^{-3}	4.2×10^{-3}	2.0×10^{-3}	5.3×10^{-3}	1.5×10^{-3}
100	9.3×10^{-3}	4.8×10^{-3}	5.6×10^{-3}	2.7×10^{-3}	3.8×10^{-3}	1.9×10^{-3}	5.3×10^{-3}	1.5×10^{-3}
200	8.8×10^{-3}	4.4×10^{-3}	5.1×10^{-3}	2.5×10^{-3}	3.3×10^{-3}	1.6×10^{-3}	3.6×10^{-3}	1.2×10^{-3}
400	8.6×10^{-3}	4.3×10^{-3}	4.9×10^{-3}	2.4×10^{-3}	3.1×10^{-3}	1.5×10^{-3}	2.2×10^{-3}	1.1×10^{-3}

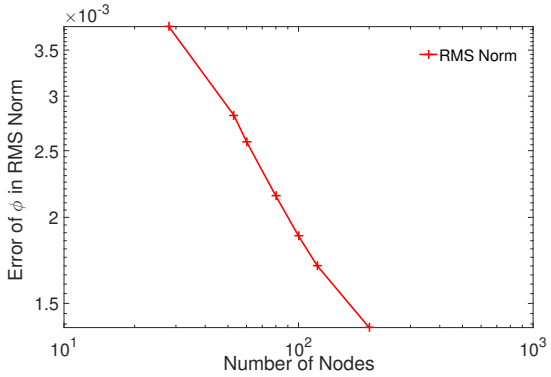

Figure 10: RMS Errors Norms: RIBEM results with spatial meshes for Pé = 1. Convergence for the concentration ϕ with increasing nodes for experiment 1.

8.1.2. Negative velocity

We now solve this problem with negative velocities to provide further validation of the proposed scheme. Figure 11 displays the solutions for $S = 10$ and $v_x = -10$. In Fig. 12 the velocity has been increased to

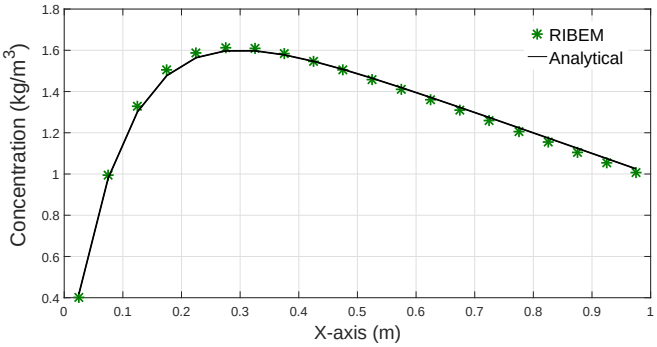

Figure 11: Variation of concentration profile ϕ along faces $y = 0$ and $y = 1$ for $S = 10$, $v_x = -10$: comparison between the analytical (solid line) and numerical (star points) solutions

$v_x = -80$ and $S = 80$. The Péclet number in this case is 80. Then, the value of S is considered as 100

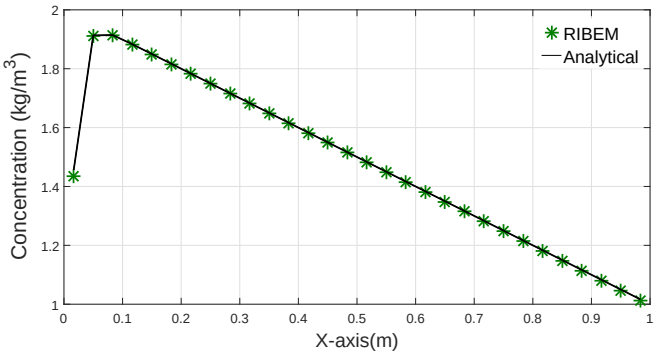

Figure 12: Variation of concentration profile ϕ along faces $y = 0$ and $y = 1$ for $S = 80$, $v_x = -80$: comparison between the analytical (solid line) and numerical (star points) solutions

to make the velocity and the concentration profiles significantly sharp in the opposite direction. Figure 13 compares the BEM and analytical solutions for this case. Once again, the results show very good agreement for a Péclet number equal to 50 in this case. Finally, Fig. 14 presents the solutions for a higher value of

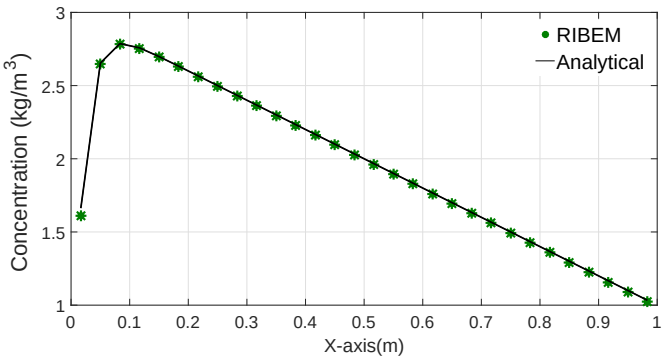

Figure 13: Variation of concentration profile ϕ along face $y = 0$ and $y = 1$ for $S = 100$, $v_x = -50$: comparison between the analytical (solid line) and numerical (star points) solutions

160

the source coefficient $S = 500$ with $v_x = -20$. Throughout this section, the figures for negative velocities

Figure 14: Variation of concentration profile ϕ along faces $y = 0$ and $y = 1$ for $S = 500$, $v_x = -20$: comparison between the analytical (solid line) and numerical (star points) solutions

show very good agreement between the numerical and the analytical solutions, for the concentration profile results at different values of the Péclet number and with different source term values. We observe that the numerical solutions are non-oscillatory and are in good agreement with the analytical solutions in all cases.

8.1.3. Convergence with spatial mesh refinement

To assess the convergence of the boundary concentration ϕ with spatial mesh refinement, we present global errors in L^∞ and RMS norms with different mesh sizes at different values of Péclet number, as presented in Table 2 and Fig. 10. The L^∞ error norm quoted is the error between the boundary concentration of the simulated and the analytical solutions. The results with these various element sizes indicate very small relative errors in L^∞ and RMS, respectively, showing very good solution behaviour and convergence for this problem.

The proposed scheme shows in Fig. 10 convergence with mesh refinement. Very small values of the relative error in the L^∞ and RMS norms have been obtained. Spatially, the solution seen in the mentioned figure converges quickly; for small and large N roughly errors of the order 10^{-3} for the L^∞ and RMS norms are observed.

8.2. Experiment 2: Two-dimensional convection-diffusion-reaction problem over a square channel and exponential diffusivity-dependent source term

Consider a convection-diffusion-reaction problem with a variable source term, subject to mixed boundary conditions: For vertical faces, i.e. $x = 0$ and $x = 1$, Dirichlet boundary conditions are imposed:

$$\phi = 1;\, x = 0,\, 0 \leq y \leq 1$$

$$\phi = 0;\, x = 1,\, 0 \leq y \leq 1$$

and zero fluxes (Neumann boundary conditions) for the horizontal faces, i.e. $y = 0$ and $y = 1$:

$$q = \frac{\partial \phi}{\partial n} = 0;\, y = 0,\, 0 \leq x \leq 1$$

$$q = \frac{\partial \phi}{\partial n} = 0;\, y = 1,\, 0 \leq x \leq 1$$

The source term varies in the form:

$$S\left(x, y\right) = \frac{2\,\mathrm{e}^{\left(\frac{1}{D}\right)}}{\left[D\,\mathrm{e}^{\left(\frac{x}{D}\right)}\left(\mathrm{e}^{\left(\frac{1}{D}\right)} - 1\right)\right]} \tag{35}$$

The analytical solution of the problem is given by

$$\phi\left(x, y\right) = \frac{\exp(\frac{-x}{D}) - \exp(\frac{-1}{D})}{1 - \exp(\frac{-1}{D})} \tag{36}$$

This case study is discretised into 120 equally spaced constant elements, 30 on each side as shown in Fig. 3. Figure 15 presents the solution with velocity $v_x = 10$ and diffusivity value $D = 100$. Table 3 shows a comparison between the simulation and the analytical solutions at different positions at the bottom side for Pé $= 0.1$. To compare the different global solutions errors, the RMS error norm is used for this case study. Figure 16 demonstrates the solution at velocity value $v_x = 0.05$ and diffusivity coefficient $D = 100$. Table 4 shows a comparison between the simulation and the analytical solutions with diffusivity value $D = 100$ and

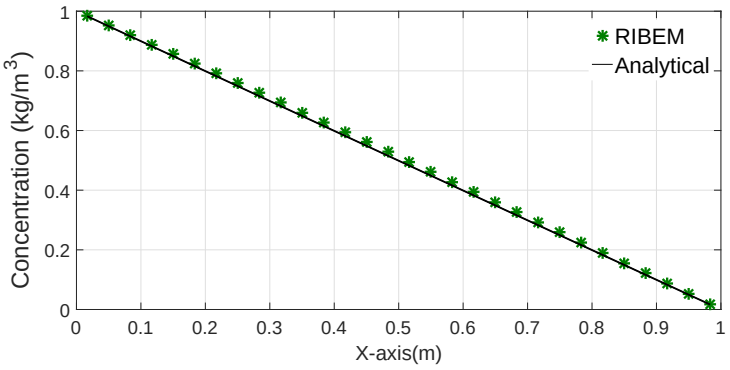

Figure 15: Variation of concentration profile ϕ along faces $y = 0$ and $y = 1$: comparison between the analytical (solid line) and numerical (star points) solutions

Table 3: Results of RIBEM for convection-diffusion-reaction problem at Pé $= 0.1$

x	RIBEM	Analytical
0.1	0.8883	0.8828
0.2	0.7912	0.7825
0.3	0.6932	0.6823
0.4	0.5944	0.5821
0.5	0.4947	0.4821
0.6	0.3940	0.3822
0.7	0.2925	0.2823
0.8	0.1900	0.1826
0.9	0.0864	0.0830

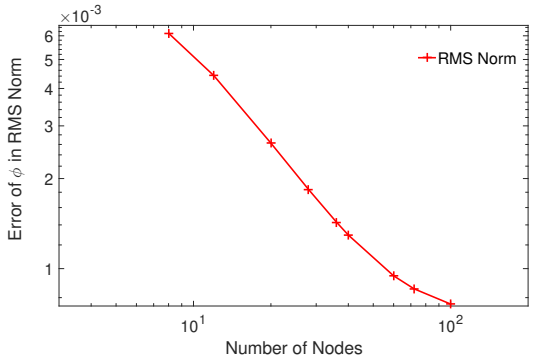

Figure 16: RMS Errors Norms: RIBEM results with spatial meshes for Pé $= 0.01$. Convergence for the concentration ϕ with increasing nodes for experiment 2.

various values of $v_x = 0.01, 0.1, 1, 10$. To assess the convergence of the concentration ϕ with spatial mesh refinement, we present L^∞ and RMS errors norms with different element sizes for different Péclet numbers

Table 4: L^∞ and RMS norms of RIBEM for convection-diffusion-reaction problem with different values of Péclet number.

Péclet number, L^∞ and RMS error norms in ϕ, Experiment 2								
Mesh size	Pé = 0.0001		Pé = 0.001		Pé = 0.01		Pé = 0.1	
	$\|e_\phi\|_\infty$	$\|e_\phi\|_{RMS}$	$\|e_\phi\|_\infty$	$\|e_\phi\|_{RMS}$	$\|e_\phi\|_\infty$	$\|e_\phi\|_{RMS}$	$\|e_\phi\|_\infty$	$\|e_\phi\|_{RMS}$
20	5.3×10^{-3}	2.5×10^{-3}	5.4×10^{-3}	2.5×10^{-3}	5.8×10^{-3}	2.6×10^{-3}	1.2×10^{-2}	6.9×10^{-3}
40	2.9×10^{-3}	1.0×10^{-3}	2.9×10^{-3}	1.1×10^{-3}	3.1×10^{-3}	1.3×10^{-3}	1.2×10^{-2}	6.6×10^{-3}
80	1.5×10^{-3}	4.4×10^{-4}	1.5×10^{-3}	4.5×10^{-4}	6.1×10^{-3}	8.1×10^{-4}	1.2×10^{-2}	6.5×10^{-4}
100	1.2×10^{-3}	3.2×10^{-4}	1.2×10^{-3}	3.4×10^{-4}	1.4×10^{-3}	7.6×10^{-4}	1.2×10^{-2}	6.5×10^{-3}
200	5.9×10^{-4}	1.3×10^{-4}	6.0×10^{-4}	1.5×10^{-4}	1.3×10^{-3}	6.9×10^{-4}	1.2×10^{-2}	6.5×10^{-3}
400	3.0×10^{-4}	5.8×10^{-5}	3.0×10^{-4}	1.0×10^{-4}	1.3×10^{-3}	6.8×10^{-4}	1.2×10^{-2}	6.5×10^{-3}

in Table 4. The accuracy of the results for the RIBEM is excellent as the L^∞ and RMS relative error norms are of the order 10^{-2} to 10^{-5} in this test case.

8.2.1. Convergence with spatial mesh refinement

To analyse the convergence of the proposed numerical method, Fig. 16 depicts the RMS relative errors of the numerical results at different meshes, obtained by using the proposed RIBEM with respect to the number of boundary elements, where the results were yielded at 120 calculation points uniformly-spaced over the relevant domain. The global errors obtained with various choices of spatial meshes for the boundary concentration ϕ in the L^∞ and RMS error norms with different element sizes at different values of Péclet numbers is presented in Table 4 and Fig. 16. The findings with these various element sizes indicate very small relative errors in L^∞ and RMS norms for all figures in this case study. Therefore, we can safely draw the conclusion that the present methodology is accurate and convergent for the computation of two-dimensional convection-diffusion-reaction problem with a variable source term.

8.3. Experiment 3: Two-dimensional non-homogeneous convection-diffusion-reaction problem over a square domain with sinusoidal (cosenoidal) source term

Next, we consider another problem whose domain is defined as a unit square. We consider the case where the source term $\mathrm{S}(x,y) = 3\sin(x) - \cos(x)$. The test case is discretised into 120 equally spaced constant elements, 30 on each side as shown in Fig. 3. Therefore, the non-homogeneous 2D convection-diffusion-reaction problem can be re-written as

$$D\nabla^2\phi - v_x\frac{\partial\phi}{\partial x} - v_y\frac{\partial\phi}{\partial y} - k\,\phi = 3\sin(x) - \cos(x) \tag{37}$$

subject to the mixed boundary conditions: For vertical faces, i.e. $x = 0$ and $x = 1$, non-homogeneous Dirichlet boundary conditions are imposed

$$\phi = \sin(0)\,;\; x = 0,\; 0 \le y \le 1$$

$$\phi = \sin(1)\,;\; x = 1,\; 0 \leq y \leq 1$$

and zero lateral fluxes (Neumann boundary conditions) for horizontal faces, i.e. $y = 0$ and $y = 1$:

$$q = \frac{\partial \phi}{\partial n} = 0;\; y = 0,\; 0 \leq x \leq 1$$

$$q = \frac{\partial \phi}{\partial n} = 0;\; y = 1,\; 0 \leq x \leq 1$$

The analytical solution of the problem is given by

$$\phi(x, y) = \sin(x) \tag{38}$$

Figure 17 shows the simulation and the exact solutions using $v_x = -1$, $k = 0$ and $D = 1$. Then, Fig. 18

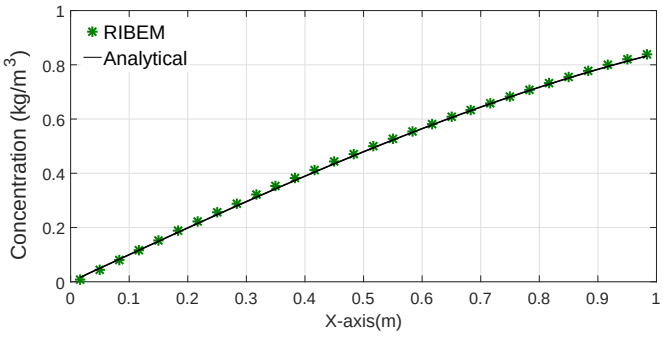

Figure 17: Variation of concentration profile ϕ along faces $y = 0$ and $y = 1$ for $v_x = -1$, $D = 1$: comparison between the analytical (solid line) and numerical (star points) solutions

presents the solutions using $v_x = -4$ and $D = 5$. It can be seen that the simulation and the exact solutions show very good agreement. Figure 19 displays the numerical solution for the concentration profile ϕ by using

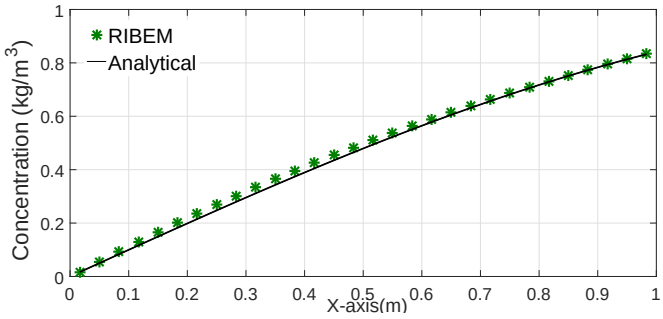

Figure 18: Variation of concentration profile ϕ along faces $y = 0$ and $y = 1$ for $v_x = -4$, $D = 5$: comparison between the analytical (solid line) and numerical (star points) solutions

$v_x = -50$ and $D = 100$. Next, Fig. 20 shows the simulation and the exact solutions using $v_x = -5$, $D = 10$ and $k = 2$.

To compare the different global solutions errors, the RMS error norm is shown in Fig. 21 for coarse and refined meshes. These error measures are computed for $v_x = -1$, $D = 1$ and $k = 0$. The plots show that the

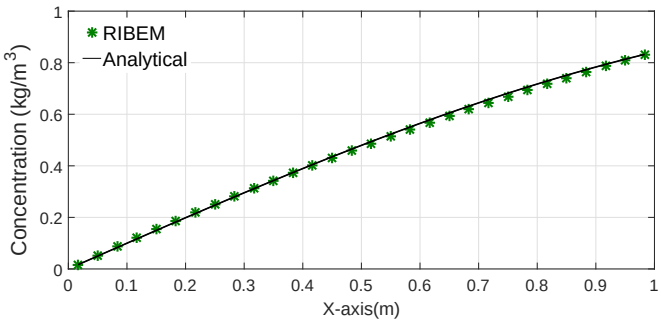

Figure 19: Variation of concentration profile ϕ along faces $y = 0$ and $y = 1$ for $v_x = -50$, $D = 100$: comparison between the analytical (solid line) and numerical (star points) solutions

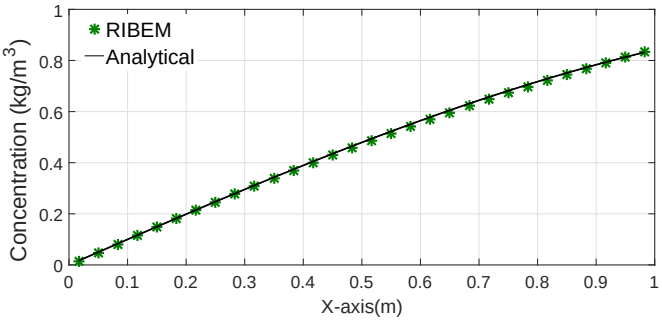

Figure 20: Variation of concentration profile ϕ along faces $y = 0$ and $y = 1$ for $v_x = -5$, $D = 10$ and $k = 2$: comparison between the analytical (solid line) and numerical (star points) solutions

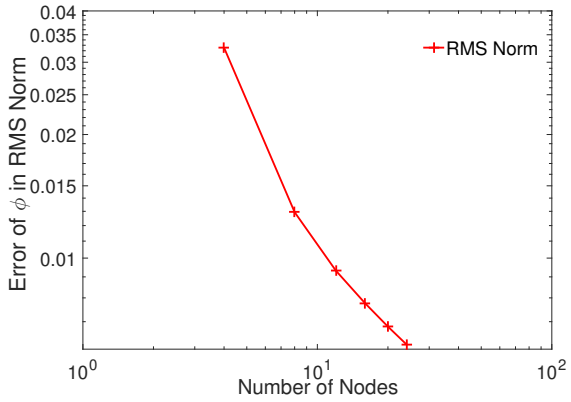

Figure 21: RMS Error Norm: RIBEM results with spatial meshes at Pé = 1. Convergence for the concentration ϕ with increasing nodes for experiment 3.

numerical solutions obtained from the present method capture the characteristic features of the analytical solution even for coarse meshes.

Table 5 shows a comparison between the simulation and the analytical solutions where $v_x = -1$, $D = 1$, $k = 0$. This table shows the same level of accuracy at different positions along the face $y = 0$.

Table 5: Results of RIBEM for convection-diffusion-reaction problem at Pé = 1

x	RIBEM	Analytical
0.1	0.1168	0.1164
0.2	0.2220	0.2150
0.3	0.3207	0.3114
0.4	0.4131	0.4047
0.5	0.4997	0.4940
0.6	0.5814	0.5783
0.7	0.6586	0.6569
0.8	0.7315	0.7289
0.9	0.7995	0.7936

Table 6: L^∞ and RMS norms of RIBEM for convection-diffusion-reaction problem with different values of Péclet number.

Péclet number, L^∞ and RMS error norms in ϕ, Experiment 3								
Mesh size	Pé = 0.001		Pé = 0.01		Pé = 0.1		Pé = 1	
	$\|e_\phi\|_\infty$	$\|e_\phi\|_{RMS}$	$\|e_\phi\|_\infty$	$\|e_\phi\|_{RMS}$	$\|e_\phi\|_\infty$	$\|e_\phi\|_{RMS}$	$\|e_\phi\|_\infty$	$\|e_\phi\|_{RMS}$
20	0.1840	0.0839	0.1424	0.0658	0.0481	0.1026	0.0152	0.0068
40	0.1610	0.0734	0.1284	0.0593	0.0934	0.0452	0.0124	0.0049
80	0.1526	0.0694	0.1210	0.0569	0.0891	0.0442	0.0099	0.0040
100	0.1510	0.0687	0.1199	0.0565	0.0885	0.0440	0.0094	0.0038
200	0.1477	0.0678	0.1175	0.0559	0.0870	0.0438	0.0090	0.0036
400	0.1461	0.0674	0.1163	0.0557	0.0862	0.0437	0.0087	0.0035

In addition, to show the convergence of the boundary concentration ϕ with spatial mesh refinement, we present L^∞ and RMS errors norms with different element sizes for different Péclet numbers in Table 6. The accuracy of the results for the RIBEM is excellent using a high value of diffusivity $D = 100$, as the L^∞ and RMS relative error norms are of order 10^{-1} to 10^{-3} for all values of the Péclet number.

8.3.1. Convergence with spatial mesh refinement

The global errors obtained for the boundary concentration ϕ in L^∞ and RMS errors norms with different mesh sizes at different values of the Péclet number are presented in Table 6 and Fig. 21. The numerical outcomes with these various element sizes indicate small relative error in both L^∞ and RMS norms with good convergence behaviour of solution as shown in all figures. The calculated relative errors are obtained in the RMS error norm and are plotted against mesh sizes in Fig. 21. It can be seen that the errors are reduced with continuous mesh refinement for low Péclet number, whereas the error is reduced by an order of magnitude for Pé=1. Further, for all spatial mesh refinement, the RIBEM for problem 3 produced an

accurate behaviour of the boundary concentration even with a small number of boundary elements.

8.4. Experiment 4: Two-dimensional non-homogeneous convection-diffusion-reaction problem over a square panel with parabolic source term

This problem has been modelled as two-dimensional over a unit square, $\Omega = \{(x_1, x_2) : x_1, x_2 \in (0, 1)\}$. The last tested case is a non-homogeneous 2D convection-diffusion-reaction problem described by

$$D\nabla^2\phi - v_x\frac{\partial\phi}{\partial x} - v_y\frac{\partial\phi}{\partial y} - k\,\phi = -2\left(3x^2 + 1\right) \tag{39}$$

We assume the diffusivity is $D = 1$, reaction coefficient $k = 2$, and the constant velocity components are $v_x = 6$ and $v_y = 0$. The analysis is conducted with a discretisation of 120 equally spaced constant elements, 30 on each face. The boundary conditions are imposed as follows:

(i) Neumann boundary conditions at the horizontal faces i.e. $y = 0$ and $y = 1$:

$$\frac{\partial\phi}{\partial n}(x, 0) = \frac{\partial\phi}{\partial n}(x, 1) = 0,$$

(ii) Dirichlet boundary conditions at the vertical faces i.e. $x = 1$ and $x = 0$:

$$\phi(1, y) = 5.5$$

$$\phi(0, y) = 0.5$$

The analytical solution of the problem can be expressed as

$$\phi(x, y) = \exp(3x)\left[\left(\frac{-7\exp(-3) + 6\cosh\sqrt{5}}{\sinh\left(\sqrt{5}\right)}\right)\sinh\left(\sqrt{5}\,x\right) - 6\cosh\left(\sqrt{5}\,x\right)\right] + \frac{3}{2}x^2 + \frac{9}{2}x + \frac{13}{2} \tag{40}$$

Table 7: Results of RIBEM for convection-diffusion-reaction problem at Pé = 6

x	RIBEM	Analytical
0.1	0.5166	0.5098
0.2	0.5409	0.5265
0.3	0.5802	0.5592
0.4	0.6478	0.6236
0.5	0.7690	0.7483
0.6	0.9923	0.9835
0.7	1.4081	1.4165
0.8	2.1842	2.1971
0.9	3.6157	3.5807

Table 7 shows that the current simulation results are in good agreement with the analytical solution. This table provides the solutions along different positions at the bottom side of the domain. The simulation

Table 8: L^∞ and RMS norms of RIBEM for convection-diffusion-reaction problem with different values of Péclet number.

Péclet number, L^∞ and RMS error norms in ϕ, Experiment 4						
Mesh size	Pé = 4		Pé = 6		Pé = 10	
	$\|e_\phi\|_\infty$	$\|e_\phi\|_{RMS}$	$\|e_\phi\|_\infty$	$\|e_\phi\|_{RMS}$	$\|e_\phi\|_\infty$	$\|e_\phi\|_{RMS}$
12	0.7817	0.3703	0.0695	0.0379	0.8693	0.3602
40	0.7511	0.3309	0.0671	0.0306	0.9066	0.3094
80	0.7522	0.3269	0.0659	0.0288	0.9319	0.3118
100	0.7513	0.3263	0.0656	0.0285	0.9280	0.3127
200	0.7485	0.3252	0.0650	0.0283	0.9377	0.3145
400	0.7484	0.3249	0.0646	0.0283	0.9402	0.3152

errors are presented in Table 8, in which it can observed that different error norms have been calculated for the present method. We can see the relative error and the convergence behaviour of this experiment are reasonable at different values of the Péclet number. Moreover, it is worth noting that the results obtained with the RIBEM are accurate with all choices of spatial meshes.

To compare the different global solutions errors, the RMS error norms are shown in Fig. 22 for coarse and refined spatial meshes at low Péclet number, i.e. Pé = 6. Further, the convergence behaviour shown

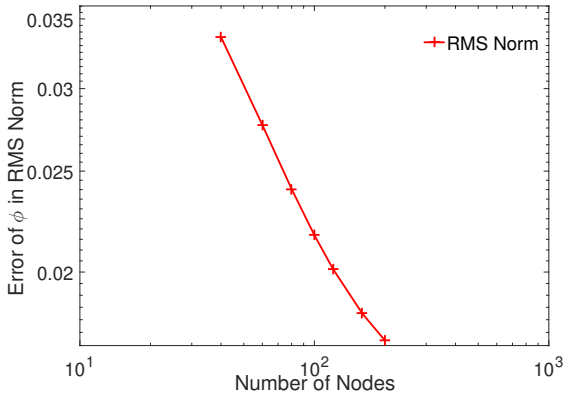

Figure 22: RMS Error Norm: RIBEM results with spatial meshes at Pé = 6. Convergence for the concentration ϕ with increasing nodes for experiment 4.

in Fig. 22 indicates that we can have a convergent solution with the RIBEM scheme. Figure 23 presents the solution using $v_x = 6$, $D = 1$ and $k = 2$. This plot shows the concentration profiles of ϕ along both horizontal faces, i.e. $y = 0$ and $y = 1$, where the predicted results for the concentration agree quite well with the corresponding analytical solutions. Figure 24 shows the simulated and the analytical solutions by considering $v_x = 10$, $D = 1.5$ and $k = 0.5$. From these figures, it can be seen that the proposed method can accurately predict the numerical solution for the convective-diffusive-reactive problem with source term.

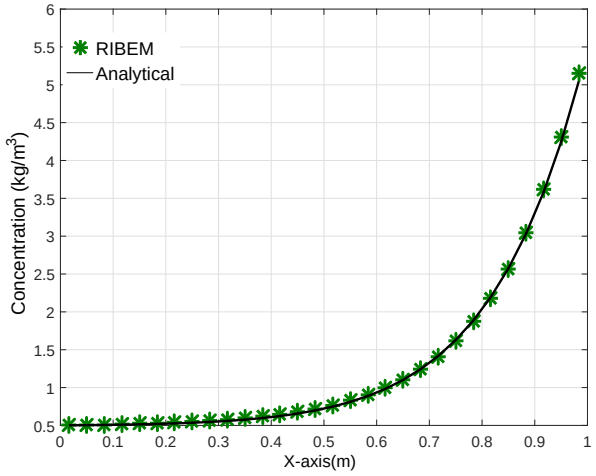

Figure 23: Variation of concentration profiles ϕ along faces $y = 0$ and $y = 1$ with $v_x = 6$, $D = 1$ and $k = 2$: comparison between the analytical (solid line) and numerical (star points) solutions

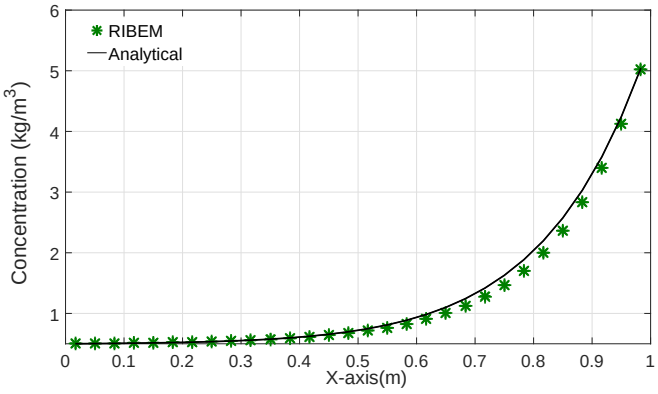

Figure 24: Variation of concentration profiles ϕ along faces $y = 0$ and $y = 1$ with $v_x = 10$, $D = 1.5$ and $k = 0.5$: comparison between the analytical (solid line) and numerical (star points) solutions

8.5. Experiment 5: Two-dimensional non-homogeneous convection-diffusion-reaction problem over a circular domain with non-linear source term

This problem has been modelled as two-dimensional over a unit disk, $\Omega = \left\{(x, y) : x^2 + y^2 \leq 1\right\}$. The last tested case is a non-homogeneous 2D convection-diffusion-reaction problem described by

$$D\nabla^2\phi - v_x \frac{\partial \phi}{\partial x} = S\,(x, y) \tag{41}$$

where $S\,(x, y)$ and the Dirichlet boundary condition are computed from the analytical solution as shown in Eq.(41):

$$\phi\,(x, y) = \exp\left(-0.5\, v_x\, x\right) \sin\left(0.5\, v_x\, y\right) \tag{42}$$

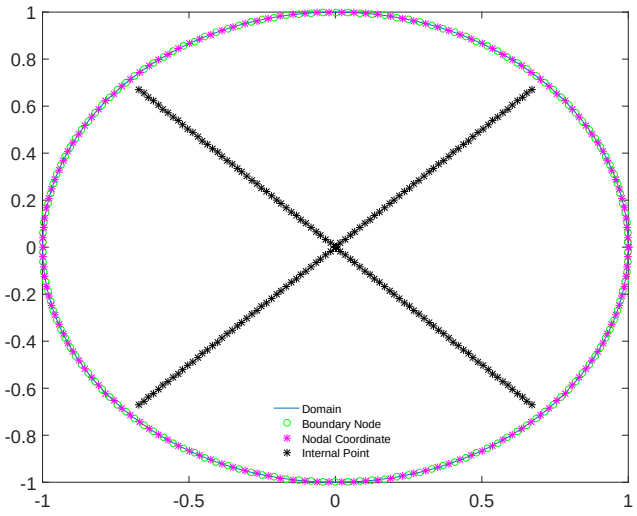

Figure 25: The computational and evaluational domain of a unit disk with 160 uniformly scattered internal points.

8.5.1. Positive velocity

Figure 26 presents the solution using $v_x = 1$, $D = 1$ and $k = 0$. The plot shows the concentration profiles of ϕ for 160 selected internal points along the diagonals where the predicted results for the concentration agree quite well with the corresponding analytical solution. The boundary is discretised into 150 constant elements.

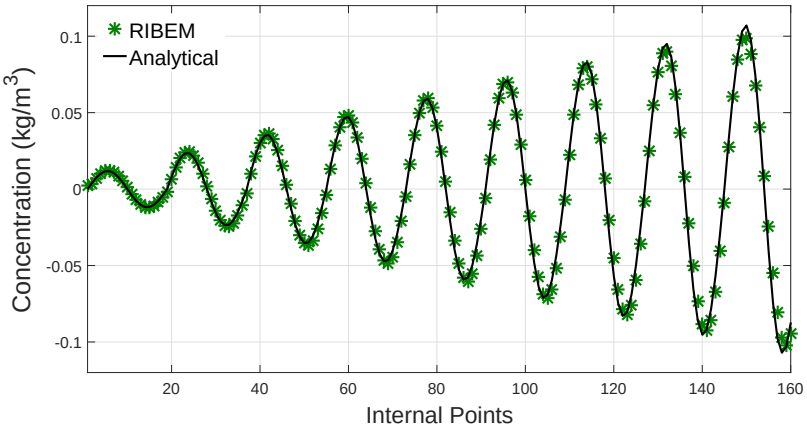

Figure 26: Variation of concentration profiles ϕ for selected internal points with positive velocity: comparison between the analytical (solid line) and numerical (star points) solutions

8.5.2. Negative velocity

Figure 27 presents the solution using $v_x = -1$, $D = 1$ and $k = 0$. This plot shows the concentration profiles of ϕ for 160 selected internal nodes along the diagonals and, once again, the predicted results for the

concentration agree quite well with the corresponding analytical solution.

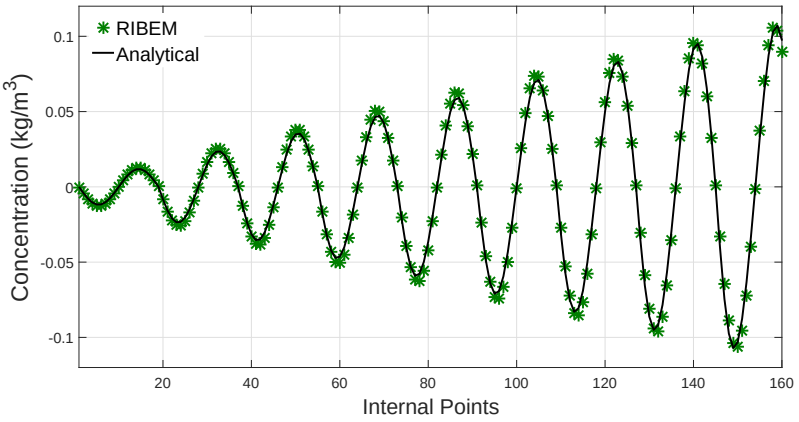

Figure 27: Variation of concentration profiles ϕ for selected internal points with negative velocity: comparison between the analytical (solid line) and numerical (star points) solutions

9. Conclusions and discussions

A new formulation of the RIBEM is developed for the two-dimensional non-homogeneous convection-diffusion-reaction problem with source term. The fundamental solution of the corresponding problem without source term is implemented in this work. The formulation is the first attempt to solving two-dimensional convection-diffusion-reaction problems with constant and variable source terms in which the BEM modelling described does not require any internal points and internal cells. The domain integral involved is transformed into equivalent boundary integral using the RIM, and a boundary-only integral equation formulation is achieved.

Numerical applications for 2D non-homogeneous problems are demonstrated to show the validity of the proposed technique, and its accuracy was evaluated by applying it to five tests with different velocity fields. Moreover, numerical results show that the RIBEM does not present oscillations or damping of the wave front as may appear in other numerical techniques.

The results presented in section 8 show the versatility of the RIBEM approach to solve non-homogeneous convection-diffusion-reaction problems involving variable source terms. We can note a distinct advantage of the present approach, which shows very good accuracy for different types of source terms. It is obvious that, as the velocity increases, the concentration distribution becomes steeper and more difficult to reproduce with numerical models.

The absolute errors in the RMS and the L^{∞} norms have been investigated in all case studies for the proposed technique. Analytical solutions are employed to examine the accuracy of the present method. Several numerical tests have been carried out to assess the performance and demonstrate the capacity to handle a wide range of situations in the context of convection-diffusion-reaction problems with source term.

10. Conflict of interest

This paper is a purely academic research, and the authors declare that there is no conflict of interests regarding the publication of this paper.

11. Acknowledgments

The authors express their sincere thanks to the anonymous referees for their valuable comments and suggestions. The first author would also like to acknowledge the Ministry of Higher Education and Scientific Research of Iraq (Al-Nahrain University) for the financial support and PhD scholarship.

References

[1] X.-W. Gao, A boundary element method without internal cells for two-dimensional and three-dimensional elastoplastic problems, Journal of Applied Mechanics 69 (2) (2002) 154–160.

[2] X.-W. Gao, A meshless BEM for isotropic heat conduction problems with heat generation and spatially varying conductivity, International Journal for Numerical Methods in Engineering 66 (9) (2006) 1411–1431.

[3] X.-W. Gao, The radial integration method for evaluation of domain integrals with boundary-only discretization, Engineering Analysis with Boundary Elements 26 (10) (2002) 905–916.

[4] M. Al-Jawary, L. C. Wrobel, Radial integration boundary integral and integro-differential equation methods for two-dimensional heat conduction problems with variable coefficients, Engineering Analysis with Boundary Elements 36 (5) (2012) 685–695.

[5] M. Cui, H.-F. Peng, B.-B. Xu, X.-W. Gao, Y. Zhang, A new radial integration polygonal boundary element method for solving heat conduction problems, International Journal of Heat and Mass Transfer 123 (2018) 251–260.

[6] M. Cui, B.-B. Xu, W.-Z. Feng, Y. Zhang, X.-W. Gao, H.-F. Peng, A radial integration boundary element method for solving transient heat conduction problems with heat sources and variable thermal conductivity, Numerical Heat Transfer, Part B: Fundamentals (2018) 1–18.

[7] S. Qu, S. Li, H.-R. Chen, Z. Qu, Radial integration boundary element method for acoustic eigenvalue problems, Engineering Analysis with Boundary Elements 37 (7-8) (2013) 1043–1051.

[8] X.-W. Gao, B.-J. Zheng, K. Yang, C. Zhang, Radial integration BEM for dynamic coupled thermoelastic analysis under thermal shock loading, Computers & Structures 158 (2015) 140–147.

[9] E. Albuquerque, P. Sollero, W. Portilho de Paiva, The radial integration method applied to dynamic problems of anisotropic plates, Communications in Numerical Methods in Engineering 23 (9) (2007) 805–818.

[10] K. Yang, X.-W. Gao, Radial integration BEM for transient heat conduction problems, Engineering Analysis with Boundary Elements 34 (6) (2010) 557–563.

[11] X.-W. Gao, An effective method for numerical evaluation of general 2D and 3D high order singular boundary integrals, Computer Methods in Applied Mechanics and Engineering 199 (45-48) (2010) 2856–2864.

[12] X.-W. Gao, W.-Z. Feng, K. Yang, M. Cui, Projection plane method for evaluation of arbitrary high order singular boundary integrals, Engineering Analysis with Boundary Elements 50 (2015) 265–274.

[13] M. Cui, W.-Z. Feng, X.-W. Gao, K. Yang, High order projection plane method for evaluation of super-singular curved boundary integrals in BEM, Mathematical Problems in Engineering 2016.

[14] W.-Z. Feng, K. Yang, M. Cui, X.-W. Gao, Analytically-integrated radial integration BEM for solving three-dimensional transient heat conduction problems, International Communications in Heat and Mass Transfer 79 (2016) 21–30.

[15] W.-Z. Feng, X.-W. Gao, An interface integral equation method for solving transient heat conduction in multi-medium materials with variable thermal properties, International Journal of Heat and Mass Transfer 98 (2016) 227–239.

[16] X.-W. Gao, W.-Z. Feng, B.-J. Zheng, K. Yang, An interface integral equation method for solving general multi-medium mechanics problems, International Journal for Numerical Methods in Engineering 107 (8) (2016) 696–720.

[17] W.-Z. Feng, X.-W. Gao, J. Liu, K. Yang, A new BEM for solving 2D and 3D elastoplastic problems without initial stresses/strains, Engineering Analysis with Boundary Elements 61 (2015) 134–144.

[18] K. Yang, W.-Z. Feng, H.-F. Peng, J. Lv, A new analytical approach of functionally graded material structures for thermal stress BEM analysis, International Communications in Heat and Mass Transfer 62 (2015) 26–32.

[19] K. Yang, H.-F. Peng, M. Cui, X.-W. Gao, New analytical expressions in radial integration BEM for solving heat conduction problems with variable coefficients, Engineering Analysis with Boundary Elements 50 (2015) 224–230.

[20] B. Zheng, X. Gao, C. Zhang, Radial integration BEM for vibration analysis of two-and three-dimensional elasticity structures, Applied Mathematics and Computation 277 (2016) 111–126.

[21] E. Albuquerque, P. Sollero, P. Fedelinski, Free vibration analysis of anisotropic material structures using the boundary element method, Engineering Analysis with Boundary Elements 27 (10) (2003) 977–985.

[22] X.-W. Gao, Boundary element analysis in thermoelasticity with and without internal cells, International Journal for Numerical Methods in Engineering 57 (7) (2003) 975–990.

[23] K. Yang, X.-W. Gao, Radial integration BEM for transient heat conduction problems, Engineering Analysis with Boundary Elements 34 (6) (2010) 557–563.

[24] K. Yang, X.-W. Gao, Y.-F. Liu, Using analytical expressions in radial integration BEM for variable coefficient heat conduction problems, Engineering Analysis with Boundary Elements 35 (10) (2011) 1085–1089.

[25] K. Yang, J. Wang, J.-M. Du, H.-F. Peng, X.-W. Gao, Radial integration boundary element method for nonlinear heat conduction problems with temperature-dependent conductivity, International Journal of Heat and Mass Transfer 104 (2017) 1145–1151.

[26] C. Zhang, M. Cui, J. Wang, X. Gao, J. Sladek, V. Sladek, 3D crack analysis in functionally graded materials, Engineering Fracture Mechanics 78 (3) (2011) 585–604.

[27] H.-F. Peng, Y.-G. Bai, K. Yang, X.-W. Gao, Three-step multi-domain BEM for solving transient multi-media heat conduction problems, Engineering Analysis with Boundary Elements 37 (11) (2013) 1545–1555.

[28] P. W. Partridge, C. A. Brebbia, L. C. Wrobel, The Dual Reciprocity Boundary Element Method, Comp. Mech. Pub., Southampton, 1992.

[29] S. A. AL-Bayati, L. C. Wrobel, The dual reciprocity boundary element formulation for convection-diffusion-reaction problems with variable velocity field using different radial basis functions, International Journal of Mechanical Sciences 145 (2018) 367–377.

[30] L. C. Wrobel, The Boundary Element Method. Applications in Thermo-Fluids and Acoustics, Vol. 1, John Wiley & Sons, Chichester, 2002.

[31] M. Aliabadi, The Boundary Element Method. Applications in Solids and Structures, Vol. 2, John Wiley & Sons, Chichester, 2002.

[32] C. A. Brebbia, J. C. F. Telles, L. C. Wrobel, Boundary Element Techniques: Theory and Applications in Engineering, Springer Science & Business Media, 2012.

[33] K. W. Morton, Numerical Solution of Convection-Diffusion Problems, Chapman & Hall, London, 1996.

[34] J. Ravnik, L. Škerget, A gradient free integral equation for diffusion–convection equation with variable coefficient and velocity, Engineering Analysis with Boundary Elements 37 (4) (2013) 683–690.

[35] X.-W. Gao, T. G. Davies, An effective boundary element algorithm for 2D and 3D elastoplastic problems, International Journal of Solids and Structures 37 (36) (2000) 4987–5008.

[36] J. C. F. Telles, A self-adaptive co-ordinate transformation for efficient numerical evaluation of general boundary element integrals, International Journal for Numerical Methods in Engineering 24 (5) (1987) 959–973.

[37] L. C. Wrobel, D. B. DeFigueiredo, Numerical analysis of convection-diffusion problems using the boundary element method, International Journal of Numerical Methods for Heat & Fluid Flow 1 (1) (1991) 3–18.

[38] D. B. DeFigueiredo, Boundary element analysis of convection-diffusion problems, Ph.D. thesis, Wessex Institute of Technology (1990).

[39] J. J. Rencis, K.-Y. Jong, Error estimation for boundary element analysis, Journal of Engineering Mechanics 115 (9) (1989) 1993–2010.